Journal of Power Sources 196 (2011) 636–643

Contents lists available at ScienceDirect

Journal of Power Sources

journal homepage: www.elsevier.com/locate/jpowsour

Interaction of coal-derived synthesis gas impurities with solid oxide fuel cell metallic components

Olga A. Marina[a,*], Larry R. Pederson[b], Christopher A. Coyle[a], Danny J. Edwards[a], Yeong-Shyung Chou[a], Carolyn N. Cramer[a]

[a] Pacific Northwest National Laboratory, Richland, WA 99352, USA
[b] North Dakota State University, Fargo, ND 58102, USA

ARTICLE INFO

Article history:
Received 28 May 2010
Received in revised form 19 July 2010
Accepted 20 July 2010
Available online 30 July 2010

Keywords:
SOFC
Metallic interconnect
Chromia-forming alloys
Passivation layer
Coal and biomass
Impurities

ABSTRACT

Oxidation-resistant alloys find use as interconnect materials, heat exchangers, and gas supply tubing in solid oxide fuel cell (SOFC) systems, especially when operated at temperatures below ~800 °C. If fueled with synthesis gas derived from coal or biomass, such metallic components could be exposed to impurities contained in those fuel sources. In this study, coupons of ferritic stainless steels Crofer 22 APU and SS 441, austenitic nickel–chromium superalloy Inconel 600, and an alumina-forming high nickel alloy alumel were exposed to synthesis gas containing ≤2 ppm phosphorus, arsenic and antimony, and reaction products were tested. Crofer 22 APU coupons coated with a $(Mn,Co)_3O_4$ protective layer were also evaluated. Phosphorus was found to be the most reactive. On Crofer 22 APU, the $(Mn,Cr)_3O_4$ passivation layer reacted to form an Mn–P–O product, predicted to be manganese phosphate from thermochemical calculations, and Cr_2O_3. On SS 441, reaction of phosphorus with $(Mn,Cr)_3O_4$ led to the formation of manganese phosphate as well as an Fe–P product, predicted from thermochemical calculations to be Fe_3P. Minimal interactions with antimony or arsenic in synthesis gas were limited to Fe–Sb and Fe–As solid solution formation. Though not intended for use on the anode side, a $(Mn,Co)_3O_4$ spinel coating on Crofer 22 APU reacted with phosphorus in synthesis gas to produce products consistent with $Mn_3(PO_4)_2$ and Co_2P. A thin Cr_2O_3 passivation layer on Inconel 600 did not prevent the formation of nickel phosphides and arsenides and of iron phosphides and arsenides, though no reaction with Cr_2O_3 was apparent. On alumel, an Al_2O_3 passivation layer rich in Ni did not prevent the formation of nickel phosphides, arsenides, and antimonides, though no reaction with Al_2O_3 occurred. This work shows that unprotected metallic components of an SOFC stack and system can provide a sink for P, As and Sb impurities that may be present in fuel gases, and thus complicate experimental studies of impurity interactions with the anode.

1. Introduction

Fuel flexibility, including the ability to operate on synthesis gas derived from coal and biomass, is among the significant advantages of solid oxide fuel cells (SOFCs) for the production of electricity [1]. With the lowering of operating temperatures to 650–800 °C for planar stacks, it has been possible to utilize cost-effective metallic materials in the place of ceramics for such components as the interconnect plate [2]. The electrical interconnect should exhibit excellent oxidation and corrosion resistance during simultaneous exposure to air and fuel, and retain high electrical conductivity as oxide scales are formed, among other attributes [2]. Transition metal-based, oxidation-resistant alloys are being most extensively considered, all of which contain active constituents (Cr, Al, and/or Si) that are preferentially oxidized at the alloy surface to form a protective scale [3]. Additional protective coatings such as $(Mn,Co)_3O_4$ spinel are often applied to the air side of the interconnect plate to minimize scale growth, though no coatings are generally deemed necessary on the fuel side of the interconnect plate.

If operated on coal-derived synthesis gas, the fuel cell stack may be exposed to multiple minor and trace impurities such as Cl, As, Cd, Hg, P, S, Sb, and Se, depending on the coal gas cleanup technology employed [4]. Many impurities, e.g., S, Se, P, Cl, are also found in biomass-derived syngas. Though anode poisoning is of principal concern [4], impurities in fuel gases may also interact with metallic tubing through which fuel is supplied, heat exchangers, and the interconnect plate. The electrical conductivity of the passivation layer and ability of that layer to protect against further oxidation are among properties that could be affected by impurity interactions. Such potential interactions have not been addressed previously.

In this study, we report interactions of As, P, and Sb in synthesis gas with four different alloys: Crofer 22 APU, a ferritic stainless steel

* Corresponding author. Tel.: +1 509 375 2337; fax: +1 509 375 2186.
E-mail address: olga.marina@pnl.gov (O.A. Marina).

0378-7753/$ – see front matter © 2010 Elsevier B.V. All rights reserved.
doi:10.1016/j.jpowsour.2010.07.081

known to form a unique $(Mn,Cr)_3O_4$ spinel top layer and a chromia sub-layer; SS 441, a ferritic stainless steel known to form chromia passivation layers; Inconel 600, an austenitic nickel–chromium superalloy that also forms chromia passivation layers; and alumel, a high nickel alloy that forms alumina passivation layers. Reaction products were identified by electron microscopy and X-ray diffraction (XRD), and compared to those expected from thermochemical calculations.

2. Experimental

2.1. Syngas with As, P, and Sb impurities

Synthesis gas was created by equilibrating H_2 and CO_2 over a commercial nickel-based catalyst to yield nominally H_2–CO–CO_2–H_2O = 30–23–21–26% at 700 °C. Phosphine (2 ppm) and arsine (1 ppm) were added from cylinders using calibrated mass-flow controllers and non-metal tubing. Antimony (1 ppm) was added as antimony vapor from a metal source via sublimation.

2.2. Test configurations

Crofer 22 APU and SS 441 ferritic steels coupons (discs 25 mm in diameter or 15 mm × 25 mm rectangles, 1 mm thick) were sealed to alumina test fixtures with a barium aluminosilicate glass at 850 °C in forming gas, and exposed to syngas containing impurities. Nickel-based alloys were tested as parts of the actual SOFC "short" (1 cell) stack, which employed an Inconel 600 heat exchanger with Inconel 600 gas supply tubes that were 50 cm long, and 0.6 cm in diameter. Alumel was evaluated in the form of a wire. Before the tests, all samples were pre-treated in air for 8–24 h at 800 °C to create stable passivation layers. Test temperatures were 700–850 °C, while times of impurity exposure ranged upwards to 650 h. All samples were cooled in dry hydrogen with no impurities present.

2.3. Post test analyses

Scanning electron microscopy with energy dispersive spectrometry (SEM/EDS) was employed to characterize reaction products. X-ray mapping was used to show elemental distributions and new phase formation. XRD was also used to identify crystal structures of alteration products.

2.4. Thermochemical calculations

Phase stability calculations were performed using HSC Chemistry 6.12 and databases contained within [5]. A baseline syngas composition defined above was used for all calculations, to which up to 10 ppm AsH_3, PH_3 or SbH_3 was added. Initial solid phases included in the calculations were chosen based on experimental observations of products formed due to syngas exposure, and included Al_2O_3, Ni, NiO, Fe, FeO, Cr_2O_3, MnO, $MnCr_2O_4$, $FeCr_2O_4$, $CoMn_2O_4$, and SiO_2. Parameters for $MnCr_2O_4$ are not included in the commercial database and were derived from Holcomb and Alman [6].

3. Results and discussion

3.1. Crofer 22 APU interactions with P, As and Sb

Exposures of Crofer 22 APU to synthesis gas in the absence of impurities P, As, or Sb at elevated temperatures resulted in no significant difference in the oxide scale formation compared to those grown in air. The as-received Crofer 22 APU plates, fabricated by rolling metal sheets down to 1 mm thickness, had a smooth surface with rms roughness below 1 μm. After exposure to clean synthesis gas at 700–850 °C for >500 h, the rms surface roughness increased to 5–10 μm, as shown in Fig. 1a. SEM/EDS analyses revealed the formation of an alteration layer consisting of two parts: a chromia sub-layer and top Mn–Cr–O. The chromia sub-layer also contained trace amounts of Fe, Al, Ti, Si, and La. The Mn–Cr–O layer, likely the $(Mn,Cr)_3O_{4-\delta}$ spinel, contained small amounts of iron, less than 0.5 at% (which is similar to the SEM/EDS sensitivity limit), either

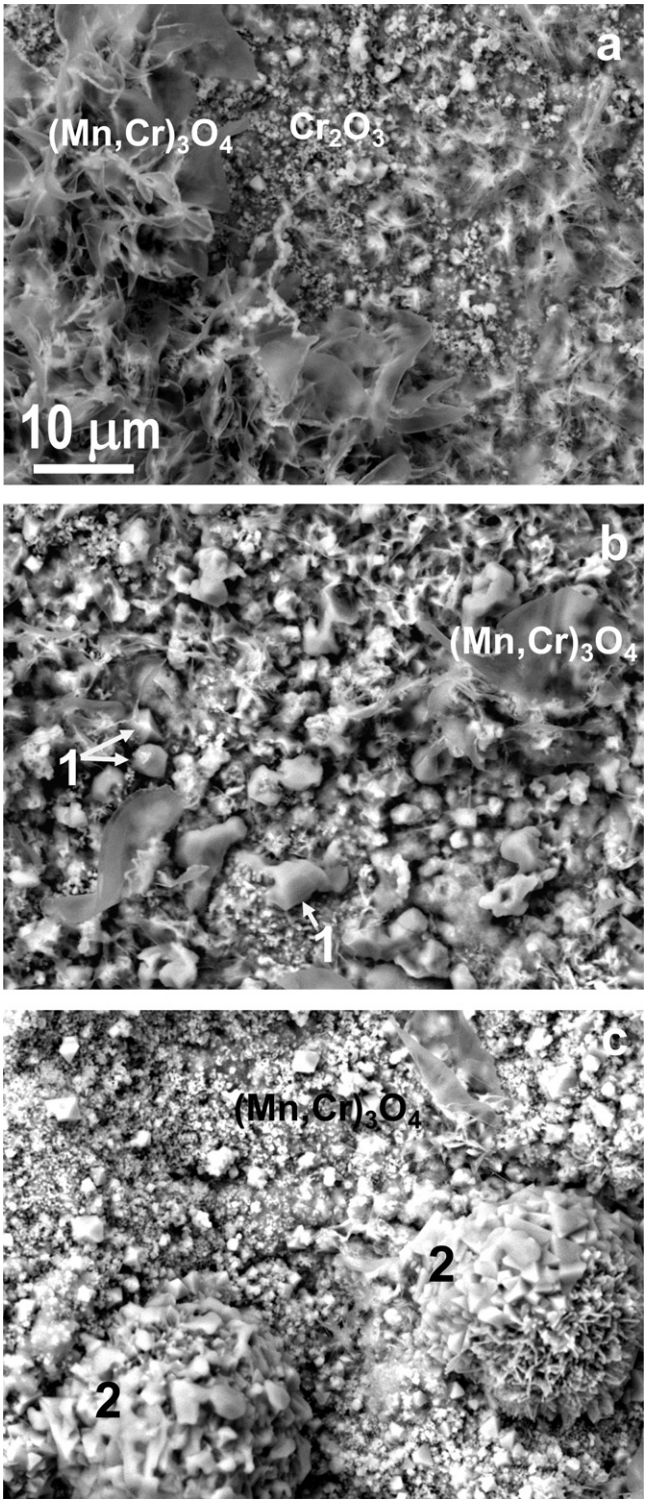

Fig. 1. SEM micrographs of Crofer 22 APU surface after exposure to (a) clean synthesis gas, and synthesis gas with (b) 1 ppm PH_3 or (c) 1 ppm Sb at 700 °C for 570 h. 1 is Mn–P–O crystals with trace amounts of Fe; 2 is Fe–Sb solid solution.

as iron oxide or $FeCr_2O_4$. While the chromia sub-layer appeared continuous and dense, the top spinel layer was non-uniform and formed irregular, small and isolated islands, and in some areas was not present at all, as shown in Fig. 1a. Longer exposures to synthesis gas did not affect the surface morphology. Such bi-layered scale structure is typical of Crofer 22 APU during exposures to air at elevated temperatures, and a dense Cr_2O_3 sub-layer with an outer layer of spinel crystals enriched in iron has been identified previously [7,8]. Therefore, exposures of Crofer 22 APU to synthesis gas at elevated temperatures resulted in no principal difference in the oxide scale formation compared to those grown in air. Moreover, since the Fe–Cr base alloys have generally exhibited higher oxidation rates in the presence of water vapor compared to dry gas [3,9], the formation of the protective scale layer in synthesis gas with high water vapor was expected. Similar conclusions have been reached by Li et al. [10] and the scale layer formed on Crofer 22 APU both in coal synthesis gas and air was attributed to the $(Cr,Fe)_2O_3$, Mn–Cr–O and Fe_3O_4 compounds. No difference in the electronic conductivity of samples exposed to synthetic coal gas or to air at 800 °C for 500 h was observed. Yang et al. [11] noticed more Fe in the scales grown on Crofer 22 APU in wet hydrogen as compared to air and suggested the $(Mn,Cr,Fe)_3O_4$ formation in the top layer in reducing environments (moist hydrogen).

When Crofer 22 APU was exposed at 700 °C to synthesis gas containing 1 ppm AsH_3, no obvious changes in the passivation layer was observed and the surface remained similar to that after exposure to clean synthesis gas. After exposures to 1 ppm PH_3 or 1 ppm Sb at 700 °C, the scale composition and surface morphology changed considerably. The surface appeared much rougher and more crystallized (Fig. 1b and c). According to X-ray elemental mapping, all interactions with impurities were limited to the upper part of the scale layer where the $(Mn,Cr)_3O_4$ spinel was present and no bulk transformations were observed. A substantial amount of phosphorus (up to 20 at%) and smaller but detectable quantities of As (<3 at%) and Sb (<5 at%) were revealed by EDS. The impurities were not distributed uniformly along the surface. As seen in Fig. 2a, after exposure to phosphorus, the spinel layer was divided into a mixture of Cr–Mn–P–O and Cr–O phases, both with small amounts of Fe. The latter, Cr_2O_3 (or Cr_2O_3–FeO–$FeCr_2O_4$ mixture since $FeCr_2O_4$ is also stable over a broad temperature range), contained no detectable amounts of phosphorus. Thus, the Cr_2O_3 layer is not reactive with phosphorus and evidently protects the bulk alloy from the deep interactions with phosphorus. The XRD analysis also suggested the presence of Cr_2O_3, $CrMn_{1.5}O_4$ or $MnCr_2O_4$, $Mn_2P_2O_7$, Fe_3O_4, and MnO. No chromium phosphates or chromium phosphides were identified by XRD, nor were iron phosphates or iron phosphides found. As and Sb were found by SEM/EDS in the localized regions in the outer spinel layer, Fig. 2b and c, indicating considerably weaker oxide layer interactions with As and Sb as compared to phosphorus. More As was detected in the areas with lower Cr content, indicating that As is likely reacted with the Cr–Mn–Fe–O phase ($MnCr_2O_4$ or $FeCr_2O_4$) rather than with Cr_2O_3 sub-layer. Because of a very low As content determined experimentally and because of the high solubility of As in Fe (6–9 at%), the formation of the Fe–As solid solution over the test period, rather than iron arsenide FeAs, is suggested [12]. When phosphorus and arsenic were present in the synthesis gas simultaneously, only phosphorus-containing compounds were clearly identified, and no arsenic compounds were determined, even after exposures to higher temperatures.

Rates of surface modification by phosphorus were accelerated at higher temperatures, Fig. 3, and the scale composition changed. While reaction products in samples tested at 700 and 800 °C could be attributed to a mixture of Cr_2O_3 and Mn–P–O (which is likely manganese phosphate $Mn_3(PO_4)_2$ or pyrophosphate $Mn_2P_2O_7$), a clearly different Cr–Mn–P–Fe–O phase was distinguished in a sample tested at 850 °C. This phase contained noticeably higher

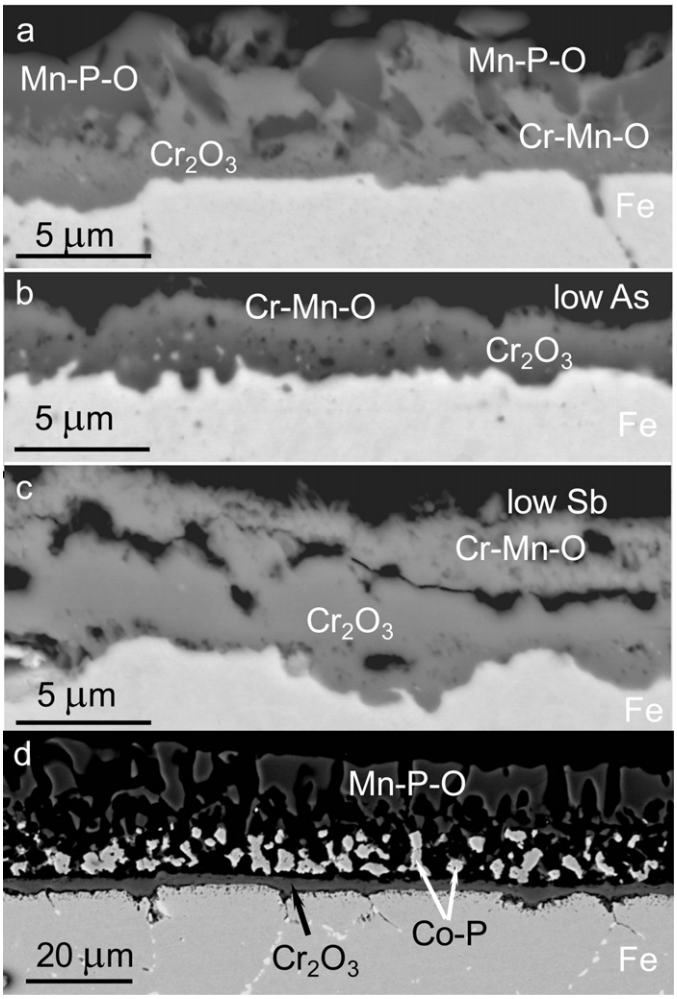

Fig. 2. Cross-sectional SEM images of polished Crofer 22 APU samples after 570 hour exposure to synthesis gas with (a, d) 1 ppm PH_3, (b) 1 ppm AsH_3, and (c) 1 ppm Sb at 700 °C. Samples a, b and c were not coated and sample d was coated with $(Mn,Co)_3O_4$.

amounts of Fe, Mn and P, while the oxygen content was lower compared to the phases in 700 and 800 °C samples. The 800 °C sample exposed to phosphorus produced distinctive surface crystals rich in iron (up to 30 at%), not observed on the surface of the 800 °C sample tested in clean synthesis gas. The 700 °C sample tested in phosphorus had no such crystals, as well. Larger quantity of such crystals, even larger in size, was found on the surface of the 850 °C sample.

Additionally, a Crofer 22 APU sample coated with the $(Mn,Co)_3O_4$ spinel was exposed to phosphorus. The presence of $(Mn,Co)_3O_4$ promoted the interactions with phosphorus, and the three different layers became distinguishable (Fig. 3d). The $(Mn,Co)_3O_4$ layer reacted with phosphorus to form a top porous Mn–P–O compound (dark gray), an intermetallic Co–P phase (light gray), while the dense Cr_2O_3 sub-layer (grey) underneath and the bulk alloy contained no phosphorus. Comparing Fig. 3a and d, both containing dense Cr_2O_3 sub-layers, it is seen that chromia serves as an effective barrier protecting the bulk Cr–Fe alloy from any interactions with phosphorus, and both $(Mn,Cr)_3O_4$ and $(Mn,Co)_3O_4$ readily reacted with P, although in a different manner.

3.2. SS 441 with P and As

Surface scale compositions and morphologies obtained on SS 441 after exposure at 800 °C to syngas gas and syngas gas contain-

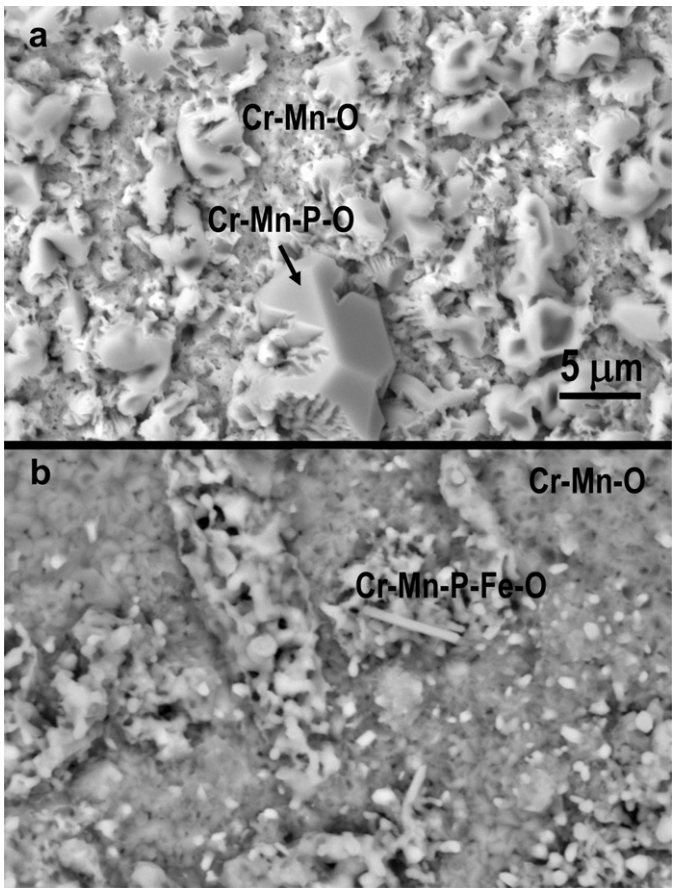

Fig. 3. SEM micrographs of Crofer 22 APU surface after exposure for 360 h to synthesis gas with 2 ppm PH_3 and 1 ppm AsH_3 at (a) 800 °C and (b) 850 °C.

ing either phosphorus or both phosphorus and arsenic were largely similar to those obtained on Crofer 22 APU (Fig. 4). The surface scale layer contained both a sub-layer of chromia and top layer of $(Mn,Cr)_3O_4$ spinel with trace amounts of Ti, Si, and Fe. This is consistent with the scale composition identified to form on other

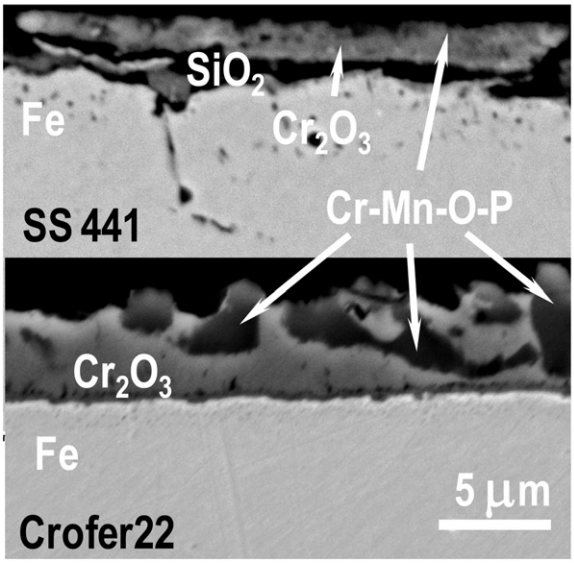

Fig. 4. Cross-sectional SEM images of polished SS 441 and Crofer 22 APU samples after exposure to synthesis gas with 2 ppm PH_3 and 1 ppm AsH_3 at 800 °C for 120 h. The chromia sub-layer has no manganese and phosphorus.

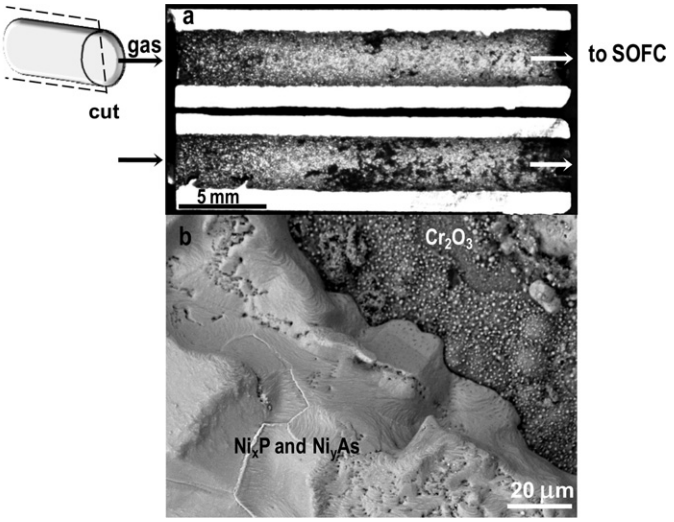

Fig. 5. (a) Cross-sectional picture of two pieces of the Inconel 600 gas supply tube after two successive 650 h tests in synthesis gas initially with 2 ppm PH_3 and then with 1 ppm AsH_3 at around 800 °C. The schematic illustrates the way that the Inconel 600 tube was cut. (b) SEM micrograph of the post test Inconel 600 surface. The dark area is mostly chromia, also with Mn–P–O. Large bright crystals are a mixture of Ni–P, Ni–As, Fe–P, and Fe–As, where the grain boundaries are rich in iron. Small round crystallites on the surface of oxide scales have the same composition as the large crystals.

similar ferritic steels, e.g., SS 430, in both air and fuel [11]. SS 441 also formed a continuous Si-rich layer near the scale/metal interface, possibly SiO_2, as seen in Fig. 4. Such a layer was not observed on Crofer 22 APU, but was found on SS 430 [11] and ZMG232 Fe–Cr alloys [13] after exposure to fuel gas. The top spinel layer on SS 441 appeared to be more uniform and continuous in comparison with that formed on Crofer 22 APU. As with Crofer 22 APU, the top spinel layer readily reacted with phosphorus to form the surface Cr–Mn–P–O compounds, likely manganese phosphate. The chromia sub-layer contained no phosphorus. No arsenic-containing compounds were detected in either chromia or spinel layers. To summarize the findings for both ferritic steels, the presence of chromia and Cr,Mn spinel scales appears to be effective in suppressing the Fe–P, Fe–As and Fe–Sb interactions and protects the bulk Fe–Cr alloy from corrosion.

3.3. Inconel 600 with P and As

A nickel–chromium superalloy, Inconel 600, was tested in the presence of phosphorus and arsenic in the form of gas supply tubes as parts of an actual SOFC test fixture. About 5 cm of the tube was cut off near the heat exchanger and split to reveal the inner part of the tube, as illustrated in Fig. 5. The SOFC stack was operated at 800 °C, while the tube temperature was maintained above 700 °C. The analyzed parts were exposed to syngas gas with 2 ppm PH_3 for 650 h, and subsequently to syngas with 1 ppm AsH_3 for 650 h. Initial heatup was performed in air, while the final cooldown was done in dry hydrogen with no impurities added.

As seen in Fig. 5, the inner part of the Inconel 600 tube underwent significant changes. Large metallic crystals formed a nearly dense metallic-like film on the surface, and the surface appeared equally altered over the whole length of the analyzed sample. A typical micrograph of the surface is given in Fig. 5b. Single point EDS analyses were performed every 4 mm from the tube end to assess the phase distribution. The dark gray surface in the upper right corner of Fig. 5b was identified as the oxide scale layer, mostly containing chromia, but also manganese (likely as $MnCr_2O_4$), iron (as FeO or $FeCr_2O_4$) and nickel (as NiO or $NiCr_2O_4$) and trace amounts

of Si and Ti. Large bright crystals in the center were attributed to the mixture of intermetallic Ni–P and Ni–As phases, likely Ni_3P, Ni_5P_2, $Ni_{12}P_5$, and Ni_5As_2, all of which were also found on the surface of the Ni/YSZ anode support inside the stack. The nickel content in this intermetallic mixture was constant over the entire sample length. The crystals also contained iron, most likely in the form of Fe–P and Fe–As, and the iron-containing phases segregated at the grain boundaries inside the Ni–P and Ni–As mixture (seen in the lower left corner in Fig. 5b). The oxygen peak was clearly present in the EDS spectra, possibly due to the presence of NiO and/or FeO. No Cr was detected in this mixture. Because the sample was not polished, the obtained EDS data could not be used reliably to suggest the exact composition. The arsenic-to-phosphorus ratio varied slightly over the length of the sample. An arsenic-rich phase with a As/P = 1.27 was determined at the end of the tube nearest the fuel gas inlet. The As/P decreased in the direction approaching the SOFC stack and a phosphorus-rich phase with a As/P = 0.9 was identified at the opposite end of the tube near the SOFC enclosure. These results suggest that both phosphorus and arsenic strongly interact with Inconel 600. A decreasing As/P ratio (in the direction opposite to the fuel inlet) indicates that nickel–arsenic interactions are stronger than nickel–phosphorus. Small round-looking inclusions on the top of the chromium oxide layer were also attributed to the mixture of Ni–As, Ni–P, Fe–P, and Fe–As.

Chromia-formed nickel alloys are known to demonstrate a lower scale growth rate (i.e., higher oxidation resistance) than ferritic stainless steels, particularly in reducing environments, and to develop scales with lower spinel content than Fe-base alloys [7,14]. Even in relatively high water vapor pressures, Horita et al. observed much slower scale growth rate on a Ni–Cr alloy 601 in comparison to Fe–Cr alloy 232 [14]. For Inconel 600, in particular, because of the lower Cr content (14–17 at%) compared to Crofer 22 APU (20–24 at%) and SS 441 (18–20 at%), a much thinner chromia scale layer is anticipated to develop. The Cr_2O_3 and $(Mn,Cr)_3O_4$ spinel scale in Ni–Cr base alloys is likely to include top layer rich in NiO or $NiCr_2O_4$ [3,10,11,15]. Because of the high Mn content (1 at%), oxide scale spallation could be also easily expected, as observed by Holcomb and Alman [6], and if so, this would lead to the bulk alloy being exposed to the environment. Yang et al. [11] observed porosity along the scale/metal interface on Haynes 230 (Ni–Cr alloy). Based on literature data, the formation of a continuous oxide scale layer (Ni and Fe free) on the surface of Inconel 600 in syngas could hardly be expected. As such, both As and P should be able to access the bulk alloy and react to form secondary phases, as was observed experimentally.

3.4. Alumel wire with P, As and Sb

Alumel wires exposed to synthesis gas at 700–850 °C formed a passivation layer rich in Ni, Al, Mn and Si, likely in the form of oxides. As determined by point EDS analysis and X-ray mapping, most of the manganese segregated to the surface of the wire due to higher Mn diffusivity, while Al and Si oxides were present in the sub-layer. Nickel (likely NiO) was found everywhere in the passivation layer with an exception of a thin Mn-rich top layer that could be either Mn oxide or the Mn_2AlO_4 compound, as suggested by Kriukiene and Tamulevicus [16]. Unlike chromium-containing alloys developing protective chromia scales, no alumina scale layer was developed on alumel in syngas. This could be due to the high steam vapor, which is known to inhibit the alumina scale formation [3].

Subsequent exposure to syngas with 1 ppm PH_3, 1 ppm AsH_3, or 1 ppm Sb led to severe surface and bulk transformations producing extensive Ni–P, Ni–As or Ni–Sb, respectively, secondary phases (Figs. 6 and 7). When both P and As were present in syngas simultaneously, a mixture of nickel phosphides and nickel arsenides was formed (Fig. 6). The intermetallic NiP_x and $NiAs_y$ were found

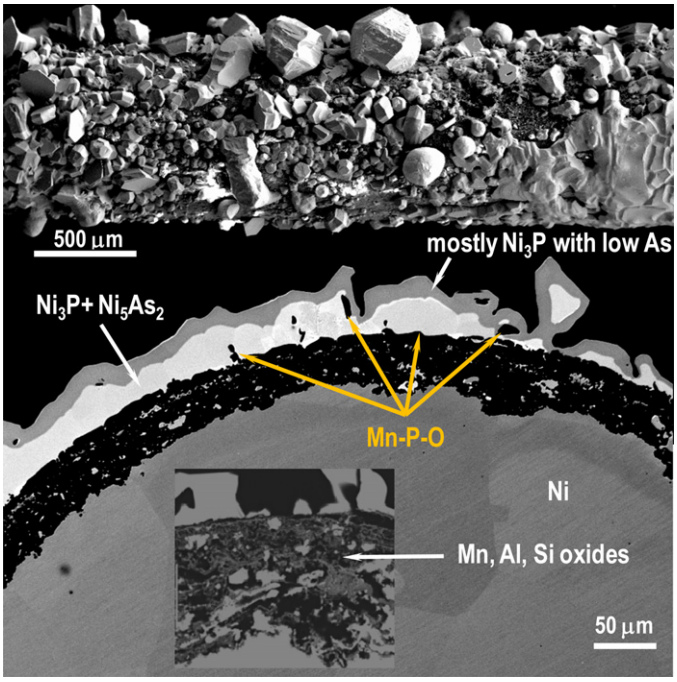

Fig. 6. SEM images of the alumel wire (top is surface, bottom is polished cross section) after exposure to synthesis gas with 2 ppm PH_3 and 1 ppm AsH_3 at 800 °C for 360 h. The insert in the bottom image shows an expanded oxide layer region.

exclusively on the outer surface, often agglomerated into large crystillites, leaving behind a non-conductive porous oxide layer fully stripped of nickel. The Mn–P–O compounds were also identified by SEM/EDS and were found mostly as an intermediate layer between

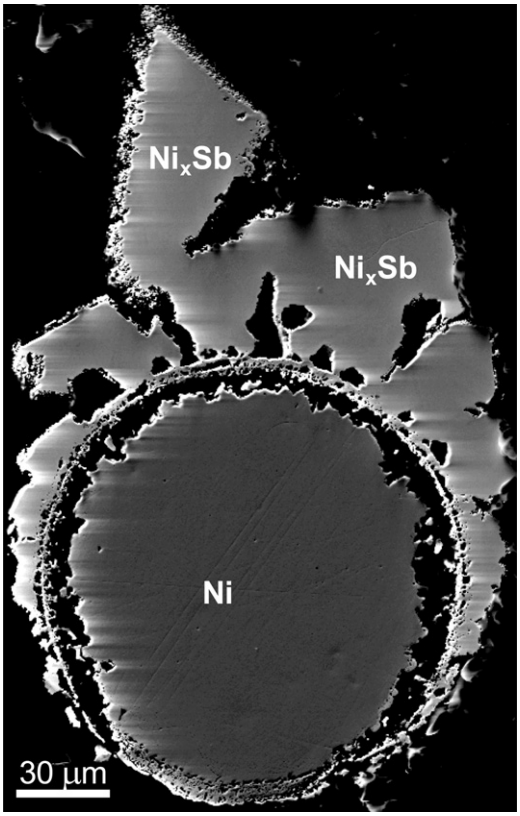

Fig. 7. SEM image of the alumel wire after 800 h test at 700 °C in synthesis gas with 1 ppm Sb.

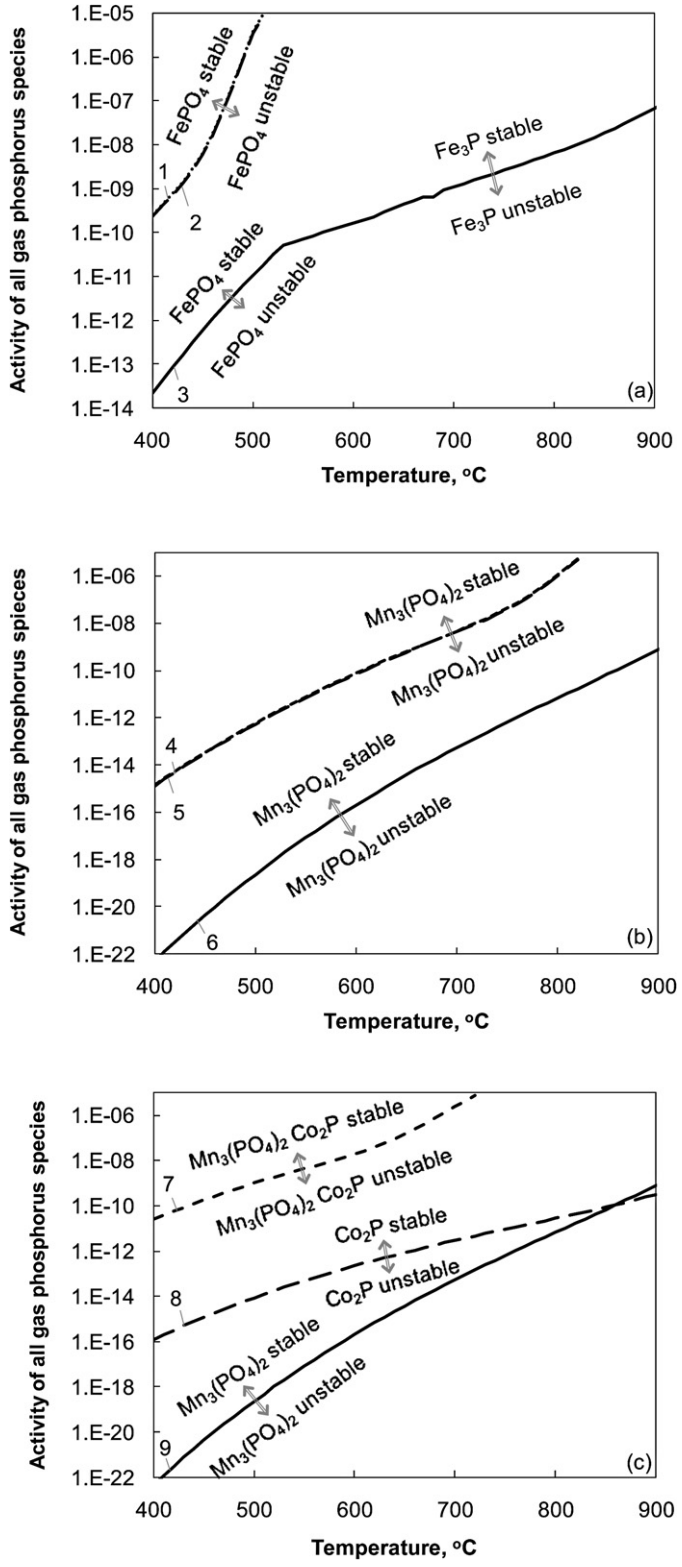

Fig. 8. Predicted activities of gas-phase phosphorus-containing species in synthesis gas with 10 ppm PH_3 (corresponding to the upper 10^{-5} limit on the *y*-axis) needed to form stable (a) $FePO_4$ and Fe_3P, (b) $Mn_3(PO_4)_2$, and (c) $Mn_3(PO_4)_2$ and Co_2P in: (1) stoichiometric $FeCr_2O_4$, (2) $FeCr_2O_4$ with excess Cr_2O_3, (3) $FeCr_2O_4$ with excess FeO; (4) stoichiometric $(Mn,Cr)_3O_4$ spinel, (5) $(Mn,Cr)_3O_4$ with excess Cr_2O_3, (6) $(Mn,Cr)_3O_4$ with excess MnO; and (7) stoichiometric $(Co,Mn)_3O_4$ spinel, (8) $(Co,Mn)_3O_4$ with excess CoO, and (9) $(Co,Mn)_3O_4$ with excess MnO.

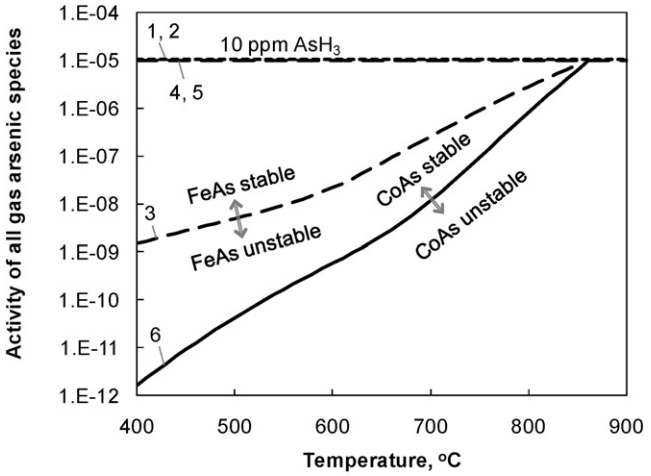

Fig. 9. Predicted activities of gas-phase arsenic-containing species in synthesis gas needed to form solid FeAs and solid CoAs in the (1) stoichiometric $FeCr_2O_4$ spinel; (2) $FeCr_2O_4$ with excess Cr_2O_3; (3) $FeCr_2O_4$ with excess FeO; (4) stoichiometric $(Mn,Co)_3O_4$ spinel; (5) $(Mn,Co)_3O_4$ with excess MnO; (6) $(Mn,Co)_3O_4$ with excess CoO. Only $FeCr_2O_4$ spinel with FeO produces FeAs and only $(Mn,Co)_3O_4$ spinel with CoO produces CoAs. Both are not stable below the corresponding lines.

the Ni_xP–Ni_yAs crystals and Al–Si oxide layer surrounding the core (Fig. 6). No Al and Si compounds with P, As, and Sb or Mn compounds with As and Sb were found. Thus, unlike dense chromia scale layer developed on Fe–Cr base alloys, the passivation layer on alumel is not effective in protecting the alloy from the interactions with P, Sb and As in synthesis gas. This could also be due to the lower than critical levels of Al in alumel required to form the protective scale at high temperatures [3].

3.5. Comparison of phases observed experimentally and predicted from thermodynamic calculations

Equilibrium calculations were performed to compare the phases observed experimentally in the passivation layers of Fe–Cr base and Ni–Cr base alloys and alumel with those expected from thermodynamic properties. Experimentally observed reaction products are summarized in Table 1, as are phases and mixtures of phases considered in the calculations. Figs. 8–10 provide predictions of

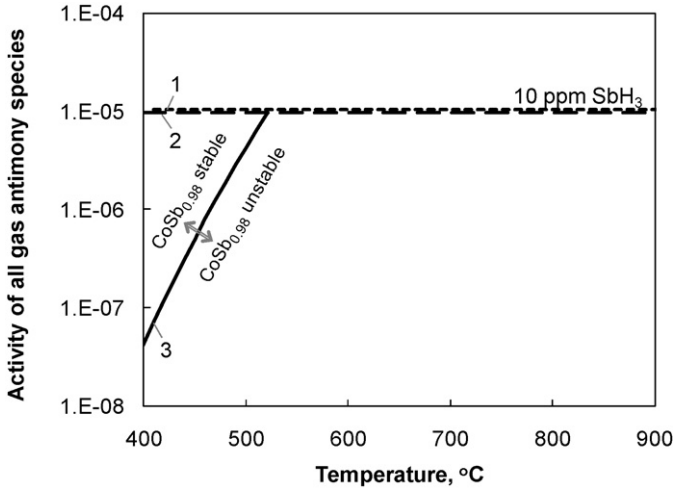

Fig. 10. Predicted activities of gas-phase antimony-containing species in synthesis gas needed to form solid Co–Sb in the (1) stoichiometric $(Mn,Co)_3O_4$ spinel; (2) $(Mn,Co)_3O_4$ spinel with excess MnO; (3) $(Mn,Co)_3O_4$ spinel with excess CoO. Only $(Mn,Co)_3O_4$ with CoO produces Co–Sb at low temperatures. Neither of the $FeCr_2O_4$ spinels, stoichiometric or with excess FeO or chromia, showed any reaction with Sb.

Table 1
Experimentally observed reaction products and phases considered and predicted from thermochemical calculations (shown in italic) in Fe–Cr base and Ni–Cr base alloy passivation layers before and after interactions with phosphorus, arsenic, and antimony in synthesis gas at 700–800 °C.

Alloy/*calculations*	Passivation layer/*phases considered*	Phases observed experimentally/*phases predicted*		
		PH_3	AsH_3	Sb
Crofer 22 APU and SS 441	$(Mn,Cr)_3O_4$	Mn–P–O	None	None
	$(Fe,Cr)_3O_4$	Fe–P	Fe–As (ss)	Fe–Sb (ss)
	Cr_2O_3	None	None	None
Coating to Crofer 22 APU	$(Mn,Co)_3O_4$	Mn–P–O Co–P	Not tested	Not tested
Inconel 600	Ni–NiO	Ni_xP	Ni_yAs	Not tested
	Fe–FeO	Fe_xP	Fe_yAs	Not tested
	Cr_2O_3	None	None	Not tested
	$(Mn,Cr)_3O_4$	Mn–P–O	None	Not tested
Alumel	Al_2O_3–MnO_x–SiO_2	NiP_x, Mn–P–O	$NiAs_x$	$NiSb_x$
Calculations	*Ni or NiO*	*Ni_3P, Ni_5P_2*	*Ni_5As_2, $Ni_{11}As_8$*	*Ni_5Sb_2, NiSb*
	Fe or FeO	*Fe_3P*	*FeAs*	*None*
	Cr_2O_3	*None*	*None*	*None*
	MnO_x	*$Mn_3(PO_4)_2$*	*None*	*None*
	$MnCr_2O_4$	*$Mn_3(PO_4)_2$*	*None*	*None*
	$MnCr_2O_4$–Cr_2O_3	*$Mn_3(PO_4)_2$*	*None*	*None*
	$MnCr_2O_4$–MnO_x	*$Mn_3(PO_4)_2$*	*None*	*None*
	$FeCr_2O_4$	*None*	*None*	*None*
	$FeCr_2O_4$–FeO	*Fe_3P*	*FeAs*	*None*
	$FeCr_2O_4$–Cr_2O_3	*none*	*None*	*None*
	$CoMn_2O_4$	*$Mn_3(PO_4)_2$, Co_2P*	*None*	*None*
	$CoMn_2O_4$–MnO_x	*$Mn_3(PO_4)_2$*	*None*	*None*
	$CoMn_2O_4$–CoO	*Co_2P*	*CoAs*	*$CoSb_{0.98}$*
	Al_2O_3	*None*	*None*	*None*
	SiO_2	*None*	*None*	*None*

(ss) is solid solution.

activities of P, As, and Sb in coal gas versus temperature over various solid phases or mixtures of solid phases considered. In agreement with experimental observations, P in coal gas is expected to be the most reactive with solid phases considered. The solids Cr_2O_3, Al_2O_3, and SiO_2 showed no tendency to form alteration phases in reactions with P, As, or Sb in coal gas.

Reactions of stoichiometric $FeCr_2O_4$ spinel and spinel with excess Cr_2O_3 or excess FeO (since both were identified by XRD) with coal gas containing phosphorus are compared as a function of temperature in Fig. 8a. Though spinels of other Fe/Cr ratios may be present, thermodynamic data for other phases were not readily available and were not considered. Iron phosphate formation is expected below ~520 °C for all cases and not at SOFC operating temperatures, whereas formation of Fe_3P is expected at higher temperature where excess FeO was present initially. Excess Cr_2O_3 is not expected to alter the reactivity of the mixture. No solid chromium phosphate or chromium phosphide formation was predicted for all three scenarios. Reactions of stoichiometric $MnCr_2O_4$ spinel, spinel with excess Cr_2O_3, and spinel with excess MnO_x versus temperature are similarly compared in Fig. 8b. Formation of the product $Mn_3(PO_4)_2$ (no data for other manganese phosphates are available in HSC) is expected in all cases, though spinel with excess MnO_x is expected to be most reactive. Comparing the experimentally observed and predicted phases, it is possible to attribute Mn–P–O phase in Fe–Cr base alloys to $Mn_3(PO_4)_2$ or $Mn_2P_2O_7$ and Fe–P to Fe_3P. The fact that Fe_3P was observed experimentally is in agreement with the XRD data supporting the presence of excess iron oxide in the chromia scale layer. Having stoichiometric $FeCr_2O_4$ without free FeO_x would not result in the formation of Fe_3P.

While stoichiometric $(Co,Mn)_3O_4$ spinel should not react with phosphorus under the SOFC conditions, Fig. 8c, both $(Co,Mn)_3O_4$ with excess CoO and $(Co,Mn)_3O_4$ with excess MnO are predicted to form solid reaction products, Co_2P in the former case and $Mn_3(PO_4)_2$ in the latter. Because both Co_2P and $Mn_3(PO_4)_2$ were observed experimentally after the test at 700 °C, one can conclude that the $(Co,Mn)_3O_4$ spinel in synthesis gas was not stoichiometric. The electrical properties of spinels are likely to be affected by the reactions with phosphorus, but were not evaluated in this study.

In the presence of As in synthesis gas, no new solid phases with chromia, manganese oxide, or $MnCr_2O_4$, such as chromium arsenate or manganese arsenate, are expected (Table 1). The formation of FeAs is expected only for the $FeCr_2O_4$ with excess FeO, but not for the stoichiometric $FeCr_2O_4$ spinel or spinel with excess Cr_2O_3 (Fig. 9). Also consistent with the experiment, the presence of expected concentrations of Sb in equilibrated syngas should not lead to the formation of Cr–Sb–O, Mn–Sb–O or Fe_2Sb solid phases (Fig. 10). Instead, the surface Fe–Sb phase was attributed to the formation of the solid solution.

4. Conclusions

Thermally grown oxide layers on Fe–Cr and Ni–Cr alloys were analyzed after exposure to synthesis gas with P, As, and Sb impurities at 700–850 °C. Chromia scales grown on ferritic steels were effective in suppressing Fe–P, Fe–As and Fe–Sb interactions. Oxide layers grown on Inconel 600 and alumel were ineffective in suppressing Ni–P, Ni–As and Ni–Sb interactions due to the presence of open porosities and Ni or NiO in the scales. Both chromium manganese spinel and cobalt manganese spinel reacted with phosphorus to produce manganese phosphate and Cr_2O_3 and manganese phosphate and Co_2P compounds, respectively. Both are likely to mitigate phosphorus reactivity in the SOFC by decreasing the total amount of phosphorus delivered to the anode. Non-chromia forming scales, including alumina, silica and manganese oxides, do not form a protective scale layer and are not effective in protecting the alloys from P, As, and Sb.

Acknowledgments

The authors would like to acknowledge G.G. Xia for providing alloy coupons, A. Schemer-Kohrn and B.P. McCarthy for performing SEM/EDS analyses, G.W. Coffey for technical assistance, and J.W. Stevenson for helpful discussions. Support for this work was provided by the US Department of Energy, Office of Fossil Energy, NETL through the SECA Coal-Based Systems Core Research Program. Pacific Northwest National Laboratory is operated for the U.S. Department of Energy by Battelle Memorial Institute under Contract AC06-76RLO 1830.

References

[1] Fuel Cell Handbook, EG&G Technical Services, U.S. Department of Energy-Office of Fossil Energy, Morgantown, WV, USA, 2004.
[2] Z.G. Yang, Int. Mater. Rev. 53 (1) (2008) 39–54.
[3] S.R.J. Saunders, M. Monteiro, F. Rizzo, Prog. Mater. Sci. 53 (5) (2008) 775–837.
[4] J.P. Trembly, R.S. Gemmen, D.J. Bayless, J. Power Sources 163 (2) (2007) 986–996.
[5] A. Roine, HSC Chemistry, 6.12 ed., Outokumpu Research Oy, Pori, Finland.
[6] G.R. Holcomb, D.E. Alman, Scripta Materialia 54 (2006) 1821–1825.
[7] Z. Yang, Int. Mater. Rev. 53 (1) (2008) 39–54.
[8] Z.G. Yang, M.S. Walker, P. Singh, J.W. Stevenson, T. Norby, J. Electrochem. Soc. 151 (12) (2004) B669–B678.
[9] D.L. Douglass, P. Kofstad, A. Rahmel, G.C. Wood, Oxid. Met. 45 (5,6) (1996) 529–545.
[10] Y. Li, J. Wu, C. Johnson, R. Gemmen, X.M. Scott, X. Liu, Int. J. Hydrogen Energy 34 (2009) 1489–1496.
[11] Z.G. Yang, G.G. Xia, M.S. Walker, C.M. Wang, J.W. Stevenson, P. Singh, Int. J. Hydrogen Energy 32 (16) (2007) 3770–3777.
[12] T.B. Massalski, H. Okamoto (Eds.), Binary Alloy Phase Diagrams, 2nd ed., ASM International, 1996.
[13] T. Horita, Y. Xiong, K. Yamaji, N. Sakai, H. Yokokawa, J. Electrochem. Soc. 150 (3) (2003) A243–A248.
[14] T. Horita, Y. Xiong, H. Kishimoto, K. Yamaji, N. Sakai, M.E. Brito, H. Yokokawa, J. Electrochem. Soc. 152 (11) (2005) A2193–A2198.
[15] S.J. Geng, J.H. Zhu, Z.G. Lu, Solid State Ionics 177 (5–6) (2006) 559–568.
[16] R. Kriukiene, S. Tamulevicus, Mater. Sci. (Medžiagotyra) 10 (2) (2004) 136–141.